Polymer-Induced Microstructure Variation in Zinc Oxide Crystals Precipitated from Aqueous Solution

Andreas Taubert,*,†,‡ Christian Kübel,§,∥ and David C. Martin§

Max-Planck-Institute for Polymer Research, Ackermannweg 10, D-55128 Mainz, Germany, and Department of Materials Science and Engineering, 2022 H. H. Dow Building, The University of Michigan, Ann Arbor, Michigan 48109-2136

The microstructure of zinc oxide particles precipitated in the presence of a poly(ethylene oxide-*block*-methacrylic acid) (P(EO-*b*-MAA)) and a poly(ethylene oxide-*block*-styrene sulfonic acid) (P(EO-*b*-SSH)) diblock copolymer was investigated. The crystals precipitated with the P(EO-*b*-MAA) copolymer consist of a region with a lower but still relatively high order close to a central grain boundary and regions of very high order further away from the central grain boundary. Selected area diffraction (SAD) found single crystalline particles in the control sample, confirmed the formation of single crystalline domains with slightly different orientations with the P(EO-*b*-MAA) copolymer, and confirmed the formation of a mosaic texture with the P(EO-*b*-SSH) copolymer. High-resolution transmission electron microscopy images exhibit little defects in the control sample. More defects are found close to the central grain boundary in the sample precipitated with P(EO-*b*-MAA). With the P(EO-*b*-SSH) copolymer, a single crystal core carries a number of lamellae, which are bent with respect to each other. Powder X-ray diffraction confirms the formation of zincite and shows a reduction of the coherence length when the crystals are precipitated in the presence of the polymers.

Introduction

Crystal engineering of inorganics has attracted interest in recent years due to its potential to obtain well-defined monodisperse particles with uniform shape and sizes in the nanometer and micrometer range. In particular, precipitation from aqueous solution has enabled the synthesis of monodisperse and uniform inorganic powders.[1−3] Several research groups have investigated the influence of synthetic polymers,[4−18] biopolymers,[19−26] and supramolecular assemblies[15,27−29] like Langmuir−Blodgett films on the crystallization of calcium carbonate, barium sulfate, and other minerals from solution.[4−10,30−42] Often uniform and monodisperse particles form in the presence of polymeric additives, thereby demonstrating the wide range of applications of the polymer-controlled crystallization.

As a result, it is now widely accepted that polymers control nucleation and crystal growth of inorganic precipitates. The mechanisms by which polymeric additives achieve control over nucleation and growth remain, however, elusive. Most studies were empirical and focused on the shape of the final particles, and only few studies[11,19,24,39,43,44] have addressed the mechanism of nucleation and crystal growth. To enable the application of polymer-controlled precipitation to various problems, it is necessary to understand in detail how polymeric additives affect the nucleation, growth, and structure of the precipitate. The correlation of crystal microstructure with the polymer structure and chemistry will then allow an understanding of polymer-controlled precipitation on a molecular level.

We have investigated the influence of a water soluble poly-(ethylene oxide-*block*-methacrylic acid) (P(EO-*b*-MAA)) and a poly(ethylene oxide-*block*-styrene sulfonic acid) (P(EO-*b*-SSH)) diblock copolymer on the internal structure and defect formation in zinc oxide precipitated from aqueous solution. Zinc oxide is a model system for controlled crystallization processes, because only one crystalline phase is observed.[45,46] This made it possible to exclusively monitor the effect of the polymers on the morphology and internal structure of the particles.

The effect of polymer composition and concentration on the morphology and internal structure of the powders was examined via powder X-ray diffraction (PXRD), scanning electron microscopy (SEM), transmission electron microscopy (TEM), and high-resolution TEM (HRTEM). The chemical nature of the polyelectrolyte block, either a poly(methacrylic acid) or a poly(styrene sulfonic acid) block, has a drastic influence on the morphology and the internal structure of the powders investigated.

Experimental Section

Materials. The P(EO-*b*-MAA) copolymer was obtained from Goldschmidt GmbH, Essen. The detailed procedure for the P(EO-*b*-SSH) copolymer synthesis is described elsewhere.[47,48] Scheme 1 shows the chemical structures, and Table 1 lists the parameters of the polymers used in this study; MAA refers to a methacrylic acid monomer unit, SSH refers to a styrene sulfonic acid monomer unit, and EO refers to an ethylene oxide monomer unit. Subscripts indicate the respective degree of polymerization. C_{12} is a $C_{12}H_{25}$ alkyl chain that is only part of the poly(ethylene oxide-*b*-MAA) copolymer. All other chemicals were of analytical grade and were used without further purification.

Crystallizations. In a typical crystallization, 446 mg of Zn-$(NO_3)_2$·$6H_2O$ (Fluka) and 12 mg of the respective polymer were

* To whom all correspondence should be addressed. Fax: +1 215 573 2128. E-mail: taubert@seas.upenn.edu.
† Max-Planck-Institute for Polymer Research.
‡ Present Address: Department of Materials Science and Engineering, 3231 Walnut St., University of Pennsylvania, Philadelphia PA 19104-6272.
§ The University of Michigan.
∥ Present Address: FEI Company, Application Laboratory, Achtseweg Noord 5, 5600 KA Eindhoven, The Netherlands.

Microstructure Variation in Zinc Oxide Crystals

J. Phys. Chem. B, Vol. 107, No. 12, 2003 **2661**

SCHEME 1: Chemical Structure of the Polymeric Additives Used in the Precipitation Reaction

a)

b)
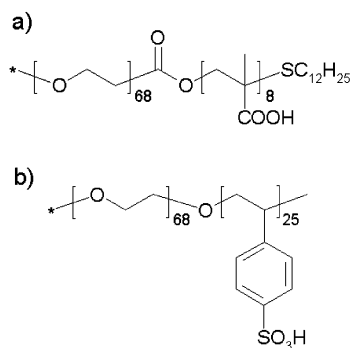
TABLE 1: Polymers Used for Precipitation Experiments[a]

polymer	M_n (g/mol) (GPC)	PD (GPC)	source
EO_{68}-b-MAA_8−C_{12}	3700		Goldschmidt
EO_{68}-b-SSH_{25}	6700	1.04	MPIP

[a] Nomenclature: M_n, number averaged molecular weight; GPC, gel permeation chromatography; PD, polydispersity; MPIP, MPI for polymer research; Goldschmidt, Goldschmidt GmbH Essen, Germany.

dissolved in 100 mL of deionized water. This solution was heated to 90 °C, and a solution of 210 mg of hexamethylene tetramine (Fluka) in 2 mL of deionized water was added to the slowly stirred solution. The mixture was allowed to react at 90 °C. The reaction was terminated after 90 min by cooling the reaction flask in an ice bath. The white precipitate was separated by centrifugation, washed with water and ethanol, and dried in a vacuum oven at 60 °C for 2 days.

SEM. Experiments were performed on dry powders deposited on conducting carbon tape without sample sputtering in a LEO 1530 SEM with a field emission gun. An acceleration voltage of 1 kV and a working distance of 5 mm were used; aperture size was 30 μm.

TEM. Powders were dispersed in 2 mL of ethanol and ultrasonicated for 5 min. Several drops of the suspension were placed on a carbon-coated copper grid and allowed to dry in air. Experiments were made on a Philips CM12 TEM equipped with a LaB_6 cathode and operated at 120 kV under low dose conditions. Data were acquired on 35 mm film (Ilford PanF). Images were digitized with a negative scanner (UMAX5000), and image analysis was performed with SISanalySIS and AdobePhotoshop5. HRTEM experiments were performed on a JEOL 4000EX TEM with a LaB_6 filament and operated at 400 kV. Data were acquired with a Gatan Imaging Filter 794 and Digital Micrograph software. Scion Image freeware[49] (Scion Corp.) was used for image analysis. HRTEM simulations were performed with the simulation program EMS Online written by P. Stadelmann, which is available online at the Centre Interdépartemental de Microscopie Electronique at the EPF Lausanne.[50] We used a zincite lattice and varied the crystal thickness from 1 to 200 nm and defoci from 0 to 200 nm. Increments were adjusted from 1 to 20 nm, depending on the overall thickness and defocus variation.

PXRD. PXRD experiments were made on a Philips PW1820 with a graphite monochromator, proportional counter, and an aluminum sample holder using Cu Kα ($\lambda = 1.5418$ Å) radiation. Background correction was performed according to ref 51 with an NBS (now NIST) zinc oxide powder as reference.

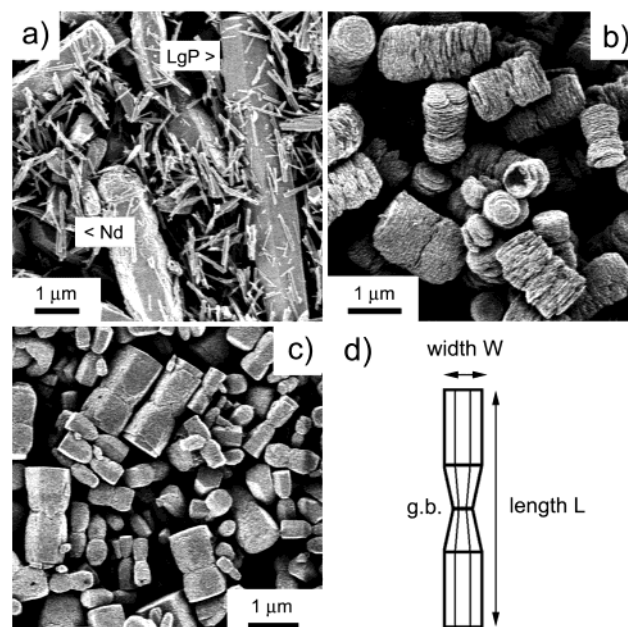**Figure 1.** SEM images of (a) the control sample with large prisms (LgP) and small needles (Nd), (b) the sample precipitated with 120 mg/L of EO_{68}-b-SSH_{25}, (c) the sample precipitated with 120 mg/L of EO_{68}-b-MAA_8−C_{12}, and (d) the definition of length, width, and grain boundary.

Results and Discussion

Sample Morphologies. As demonstrated earlier in detail,[48] both the polymer composition and the concentration have a significant influence on particle morphologies, sizes, and size distributions (Figure 1). The control sample, which was precipitated without polymer, consists of large hexagonal prisms and small needlelike particles. With EO_{68}-b-SSH_{25}, the particles resemble a "stack of pancakes". The particles of the sample precipitated with 120 mg/L of EO_{68}-b-MAA_8−C_{12} are hexagonal prisms with a rather narrow size distribution. All crystals except for the needles in the control samples exhibit a central grain boundary that was earlier assigned to twinning.[48]

PXRD. All samples consist of pure zincite (Figure 2a), and all patterns exhibit line broadening (Figure 2b). The line broadening effect is strongest for the (0002) reflections of the polymer-containing samples; we will therefore focus on the analysis of the 0002 (i.e., the crystallographic c-axis) and on the $10\bar{1}0$ (i.e., the crystallographic a-axis) reflections for comparison.

Line broadening may arise from several types of lattice imperfections that reduce the average dimension of single domains in the crystal. The size of these domains is usually calculated via the Scherrer formula[52] and discussed in terms of "crystallite size" or "coherence length" L_{hkl}.[51−53] Table 2 summarizes the experimental (B) and the background-corrected line broadening (β) and the corresponding $10\bar{1}0$ and 0002 coherence lengths of the samples displayed in Figure 1. It also shows the ratio of the $10\bar{1}0$ and 0002 coherence lengths, hence the ratio of the crystallographic a- to the crystallographic c-direction. The $10\bar{1}0$ coherence lengths of the three samples are approximately equal.

The 0002 coherence lengths of both samples precipitated with 120 mg/L of a polymeric additive are much smaller than in the control sample. The 0002 coherence length of the control sample is beyond the applicability of the Scherrer formula;[52] this indicates that the polymers preferentially induce defects on the basal planes of the growing crystals because they reduce L_{0002}
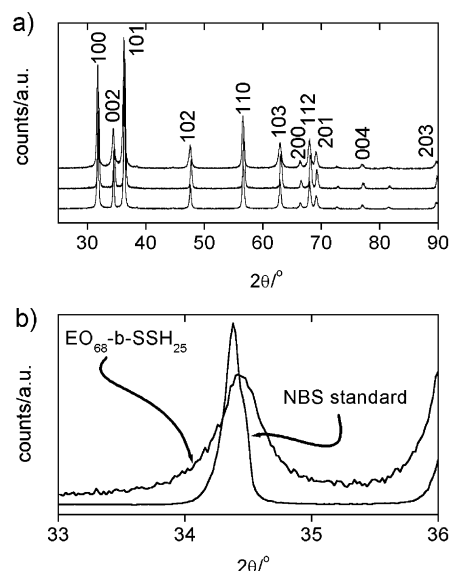
Figure 2. (a) WAXS patterns of the samples shown in Figure 1. From bottom to top: control sample, 120 mg/L EO_{68}-*b*-MAA_8−C_{12}, 120 mg/L EO_{68}-*b*-SSH_{25}. (b) Line broadening of the 0002 reflection of a sample precipitated with 120 mg/L of EO_{68}-*b*-SSH_{25}.

TABLE 2: Experimental (*B*) and Background-Corrected (*β*) Line Broadening of the 1010 and 0002 Reflections, Estimated Coherence Lengths, and *a/c* Ratios for the Samples (A−C) in Figure 1

sample	$C_{polymer}$ (mg/L)	101̄0 (*a*-direction)			0002 (*c*-direction)			
		B (°)	*β* (°)	*L* (nm)	*B* (°)	*β* (°)	*L* (nm)	*a/c*
NBS ZnO	0	0.1586			0.1590			
control	0	0.2537	0.0951	99	0.1987	0.0397	210	0.5
EO−SSH	120	0.2647	0.1061	88	0.4078	0.2488	33	2.7
EO−MAA	120	0.2638	0.1052	89	0.2785	0.1195	69	1.3

(the crystallographic *c*-axis). The effect is more pronounced for EO_{68}-*b*-SSH_{25}.

Earlier data[8,10,48] suggest that the polymers adsorb onto the basal plane because the crystals precipitated in the presence of diblock copolymers show a reduced particle length as compared to the large crystals of the control samples. The current PXRD data support these data because the coherence lengths of the crystallographic *c*-direction are much smaller with the polymeric additives than in the control sample. The differences of the *a/c* ratios (Table 2) also imply that the relative growth rate along the crystallographic *a*-axis is changed by the polymer addition. This is because the polymers reduce the overall growth rate along *c* (yielding shorter crystals) but do not reduce the width significantly.[48] Hence, the relative growth rate along the *a*-direction seems to be increased.

TEM. The large hexagonal prismatic crystals of the control sample and the particles crystallized with 120 mg/L of EO_{68}-*b*-MAA_8−C_{12} both have well-defined crystal edges and the central grain boundary is clearly visible (Figure 3a,b). Selected area electron diffraction (SAD), however, finds that the control sample almost exclusively consists of single crystals but none of the polymer-containing particles is single crystalline.

The diffraction patterns of the particles crystallized with 120 mg/L of EO_{68}-*b*-MAA_8−C_{12} crystals indicate the presence of multiple domains with an orientation distribution of ~5−10° as measured from the SAD pattern (Figure 3b). This is consistent with a preferred polymer adsorption[10,48,54] on the basal plane leading to the preferred formation of defects on the (0001) planes and subsequently to the formation of several domains and the reduction of the coherence lengths as measured from PXRD.
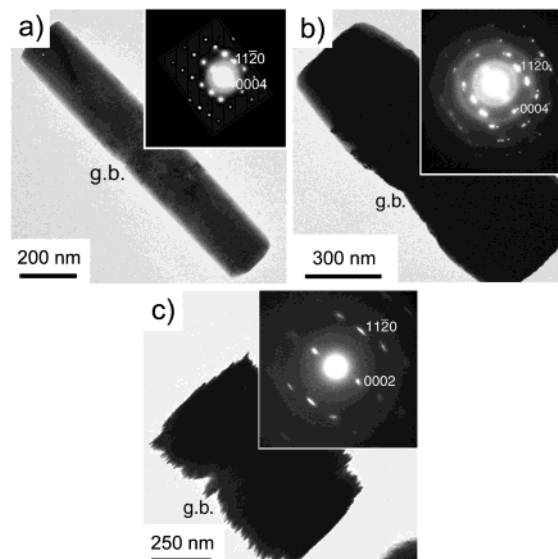

Figure 3. TEM BF images and corresponding SAD patterns of (a) the control sample, (b) a crystal precipitated with 120 mg/L of EO_{68}-*b*-MAA_8−C_{12}, (c) the crystal precipitated with 120 mg/L of EO_{68}-*b*-SSH_{25}.
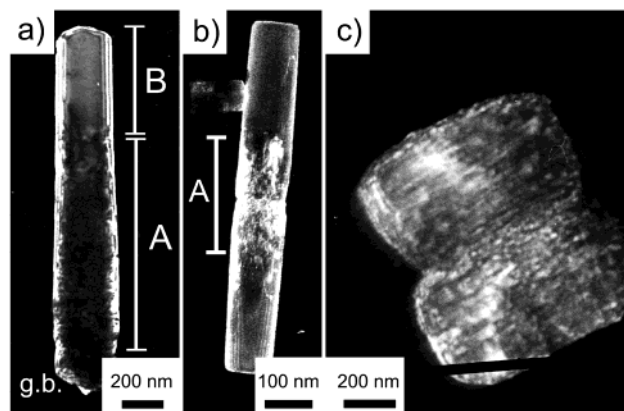

Figure 4. TEM DF images from the 112̄0 reflection, [11̄0] zone axis: (a) control sample, (b) crystal precipitated with 120 mg/L of EO_{68}-*b*-MAA_8−C_{12}. This crystal is slightly tilted so that the central grain boundary and the low-order region appear bright. The lines at the crystal edges are thickness fringes. A indicates the low-order region, and B indicates the high-order region discussed in the text. (c) Crystal precipitated with 120 mg/L of EO_{68}-*b*-SSH_{25}.

Samples precipitated with 120 mg/L of EO_{68}-*b*-SSH_{25} (Figure 3c) exhibit the same central grain boundary but very thin lamellar features rather than clear crystal faces. Individual lamellae are not in perfectly parallel orientation with respect to others, which explains the corresponding SAD patterns indicating a mosaic structure.

Dark field (DF) images of large crystals of the control sample (Figure 4a) show two different regions in the crystal. Whereas one region (A) closer to the central grain boundary exhibits some disorder at the edge of the particle, the region further away from the grain boundary (B) is of more uniform brightness. A similar observation is made for crystals precipitated with 120 mg/L of EO_{68}-*b*-MAA_8−C_{12} (Figure 4b). DF images of these crystals show large uniform domains of the same brightness at the outer parts of the crystal and a region with variable brightness close to the central grain boundary (A). The brightness variations are much more pronounced here than in the control sample. Tilting of the crystals in the TEM about their long axes revealed different parts of the crystals that appeared bright and dark depending on the Bragg condition at a certain angle. This is
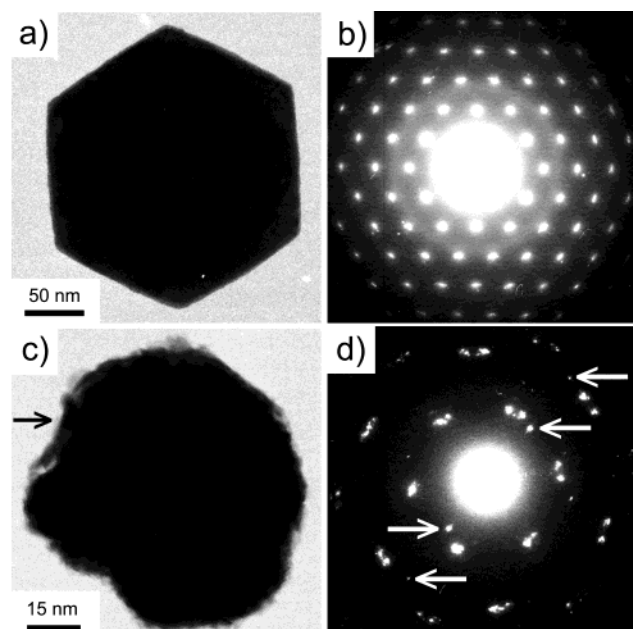
Microstructure Variation in Zinc Oxide Crystals

J. Phys. Chem. B, Vol. 107, No. 12, 2003 **2663**

Figure 5. TEM BF images and [0001] zone axis SAD patterns of a control sample (a and b) and a crystal precipitated with 120 mg/L of EO_{68}-*b*-SSH_{25} (c and d). Arrows in panel d point to non-[0001] reflections (see text).

Figure 6. TEM DF image of a crystal precipitated with 120 mg/L of EO_{68}-*b*-SSH_{25} (($1\bar{1}00$) reflection, [001] zone axis) showing rotation moirés.

more pronounced close to the central grain boundary and indicates that the crystals are highly ordered at a further distance from the central grain boundary but have a region close to the grain boundary with a somewhat lower long-range order. The domain size close to the grain boundary was ∼5−15 nm for the sample precipitated with 120 mg/L of EO_{68}-*b*-MAA_8−C_{12}.

The order increase with increasing distance from the grain boundary is presumably due to a fast initial growth regime, followed by a much slower growth regime after some of the Zn^{2+} has been removed from the solution. The high correlation even in the region close to the central grain boundary may arise from intrinsic electric fields of the nanoparticles' polar crystal lattice.[39] This first process would then be kinetically controlled, whereas the second, more highly ordered domains form via a crystal growth process limited by the diffusion of ions to the surface yielding highly correlated areas further away from the grain boundary. Hulliger and co-workers[55−59] predicted the above-presented variation in crystal order for several polar organic crystals. Their theoretical data find an increase in the order with increasing distance from a central grain boundary; this is consistent with our DF images of the control samples and with EO_{68}-*b*-MAA_8−C_{12}. Alternatively, the first precipitation step proceeds via the preciptation of nanoparticles that then aggregate, follwed by crystal growth as descrived above. This would then be similar to a model proposed by Banfield and co-workers,[19] who suggested that TiO_2 nanoparticles aggregate in a highly controlled manner, yielding larger TiO_2 crystals.

With EO_{68}-*b*-SSH_{25}, no separation into a highly ordered and a less ordered domain was found. Instead, the crystals exhibit a quite uniform distribution of dark and bright speckles over the whole particle. These crystals form via a different process[54] that involves an intermediate precipitate, which lowers the supersaturation very effectively but dissolves to leave pure zincite at longer reaction times. The implications of this reaction mechanism are reflected in the structure, which will be discussed in greater detail below.

SAD patterns of upright standing crystals confirm the results presented above for the [0001] zone axis (Figure 5). Control
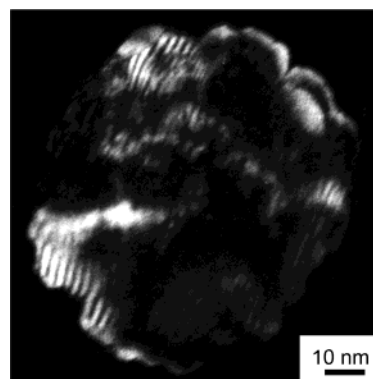
sample crystals exhibit single crystal diffraction patterns. By tilting the crystals precipitated with 120 mg/L of EO_{68}-*b*-MAA_8−C_{12}, several [0001] zone axis patterns were found. These multiple patterns correspond to the multiple [$1\bar{1}00$] zone axes identified in the previous orientation in Figure 3c. With 120 mg/L of EO_{68}-*b*-SSH_{25}, several [0001] patterns can be identified at the same time. These crystals therefore consist of several domains with different rotational orientations contributing to the diffraction pattern.

Sometimes, also a set of non-[0001] zone axis reflections are found in the pattern. These reflections arise from regions that have a completely different orientation than the majority of the crystal. We were not able to properly index these additional reflections because only few reflections were found. It is therefore unclear if these reflections point to an aggregation-based growth mechanism similar to the one suggested by Banfield and co-workers[19] or if these reflections are caused by single lamellae that simply happen to have a different orientation because the polymer adsorbed on the crystal surface prevented their proper alignment. DF images obtained from the [0001] zone axis of the sample precipitated with EO_{68}-*b*-SSH_{25} show moiré patterns (Figure 6). They are considered rotation moirés because the corresponding SAD patterns show several equivalent reflections that are slightly displaced with respect to each other (Figure 5d). From the line distance in the moiré patterns, we calculated a rotational misfit of ∼5−7°.[60] This is in good agreement with the rotation calculated from SAD patterns and indicates that in these crystals whole regions can rotate relative to one another without disrupting the highly correlated structure of the particle.

HRTEM. HRTEM images of the control sample show that the crystals contain very few defects and are single crystalline, as was anticipated from the SAD patterns (Figure 7). The observed defects are predominantly edge dislocations with Burgers vectors parallel to [0001]. Even close to the grain boundary, very few defects are found.

The defect distribution in the crystals precipitated with 120 mg/L of EO_{68}-*b*-MAA_8−C_{12} is not constant over the crystal (Figure 8). Close to the central grain boundary, more defects are found than further away from the central grain boundary. The black arrowheads in Figure 8b point to regions in the crystal interpreted as grain boundaries (not the macroscopic central grain boundary) originating from imperfect attachment of nanosized particles to each other. These microscopic grain boundaries are indicative for particle formation via association of nanocrystals rather than via crystal growth.[19,43,44]

At later reaction stages, the crystals grow via the addition of ions rather than via nanoparticle aggregation, which leads to

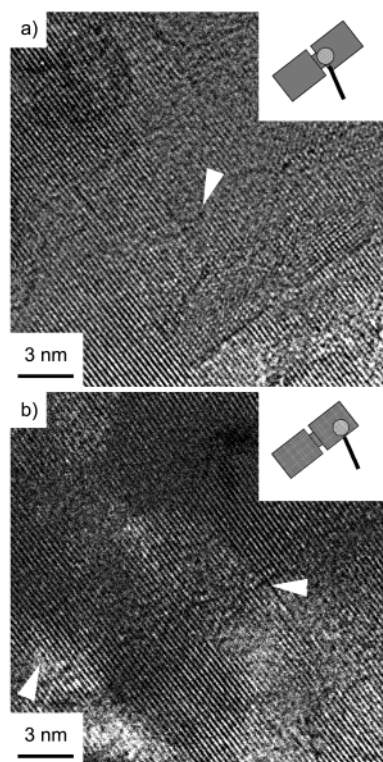**2664** *J. Phys. Chem. B, Vol. 107, No. 12, 2003*

Taubert et al.

Figure 7. HRTEM images of a control sample crystal. The magnifying glass indicates the approximate location of the image. Only selected defects are highlighted.

the higher order further away from the central grain boundary and a decrease in defect number. Further away from the central grain boundary, predominantly edge dislocations with Burgers vectors parallel to [0001] are found. HRTEM images also show that the lattice fringes are not interrupted by the central grain boundary, i.e., the crystallographic correlation persists across the boundary.

HRTEM images of the sample precipitated with 120 mg/L of EO_{68}-b-SSH_{25} reveal that the defects on the (0002) planes as suggested by PXRD are not linearly distributed within the crystal. The order in the crystal core is very high even close to the central grain boundary, i.e., the central part of the crystal contains only few defects. This is equivalent to a large coherence length, since the average defect−defect distance determines the coherence length. The small coherence length found in PXRD is due to the lamellar regions at the crystal surface (Figure 8d) because these regions are only ~10 nm thick, which leads to a significant reduction in the mean coherence length of the sample.

Figure 8e is the same image as Figure 8d but was Fourier-filtered using the (0002), (0004), (0006), and (0008) reflections. After contrast enhancement, Figure 8e was obtained. We are aware of the fact that Fourier filtering may introduce defects that are actually not present in the original image. However, Figure 8e clearly shows that the crystal consists of regions with different orientations in the outer lamellar region (but not in the central core part): The arrows are drawn perpendicular to the lattice fringes in the corresponding highlighted areas. It is clearly visible that these arrows and hence the lattice fringes have a different orientation, thus indicating a tilt of the regions with respect to each other therefore giving rise to the observed SAD pattern.

We performed HRTEM simulations in order to obtain information about thickness and defocus dependence of the visibility of the lattice fringes. The results of a HRTEM simulation are shown in Figure 9. We varied the crystal
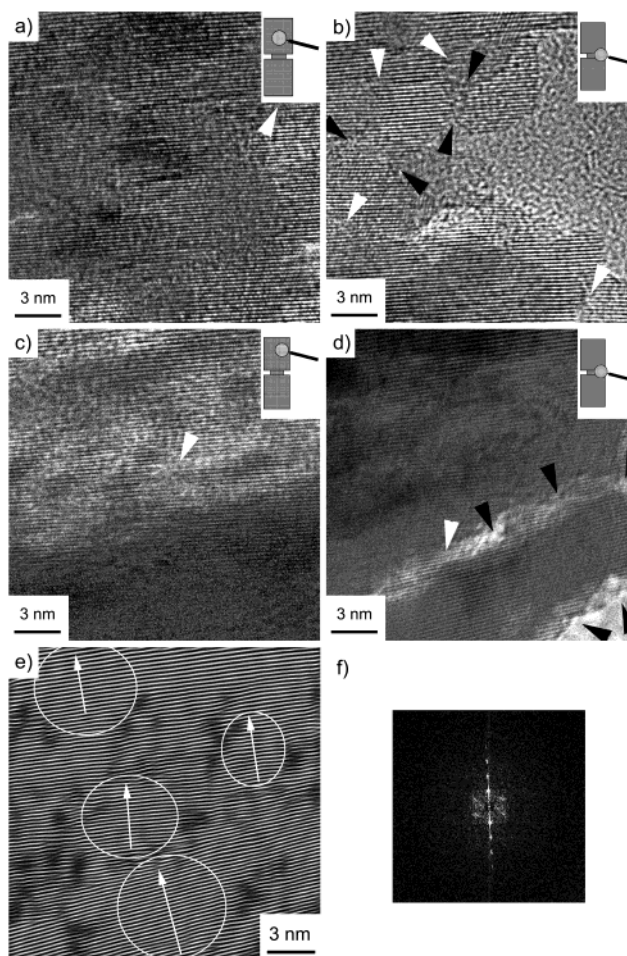

Figure 8. HRTEM images of (a, b) a sample precipitated with 120 mg/L of EO_{68}-b-MAA_8−C_{12} and (c, d) a sample precipitated with 120 mg/L of EO_{68}-b-SSH_{25}. The magnifying glass indicates the approximate spot where the image was taken. Only selected defects (white arrowheads), grain boundaries between aggregated nanoparticles (black arrowheads, Figure 8b), and lamellar boundaries (black arrowheads, Figure 8d) are highlighted. (e) Panel d after Fourier filtering and (f) corresponding power spectrum.
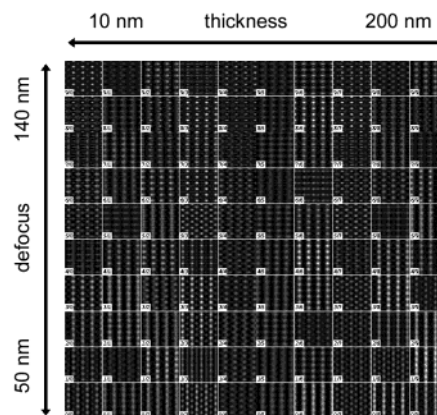

Figure 9. HRTEM simulation of the [1$\bar{1}$0] zone of a defect free zincite lattice.

thickness from 10 to 200 nm and the defocus from 50 to 140 nm for a defect free zincite lattice. Figure 9 clearly demonstrates that the contrast strongly depends on the defocus and thickness of the sample. Although these results do not provide absolute evidence that the absence of lattice fringes in certain areas is due to thickness or defocus variations, they demonstrate that sample thickness has a very significant influence on the visibility
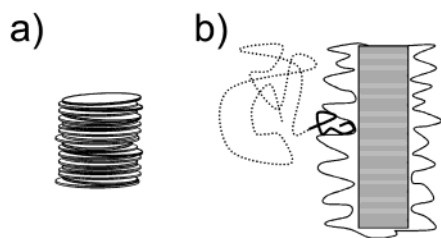
Microstructure Variation in Zinc Oxide Crystals

J. Phys. Chem. B, Vol. 107, No. 12, 2003 **2665**

Figure 10. Stack of pancakes (a) vs corn on the cob (b) structure.

of the fringes. Therefore, lattice fringes might be invisible due to a combination of defocus and thickness that leads to very low contrast and hence to the disappearance of the fringes in certain areas.

The crystals precipitated with EO_{68}-b-SSH_{25} are less perfect in regions with lamellar features and where the lamellar features have an orientation distribution. This holds for an increasing distance not from the grain boundary but from the inner core of the crystal toward its side faces (the $\{10\bar{1}0\}$ faces). HRTEM thus clearly demonstrates a transition from a very highly ordered single crystal bulk particle to a series of thin, defect-rich, and locally misoriented lamellae connected to the central single crystalline bulk crystal.

This two region structure is in agreement with kinetic experiments[54] demonstrating that first a metastable intermediate forms, followed by a central hexagonal particle. Only at later stages do the lamellae start growing away from the hexagonal particles. The central particle corresponds to the single crystalline region observed here. The polymer can only adsorb at the side faces of the core crystals after it is released from the intermediate. This adsorption step leads to the $\sim$10 nm thin lamellar features because the crystals can only grow where no polymer is adsorbed on the surface. The adsorbed polymer eventually induces a slight misorientation of the lamellae, which in turn introduces defects in the lamellae.

As a result, the stack of pancakes model actually is inaccurate in terms of the complete particle structure. Although the *morphology* is similar to a stack of pancakes, the *structure* is better described by a corn on the cob-like structure, where the single crystalline inner part holds the lamellae together (Figure 10). As a consequence, the PXRD and SAD data may be explained in the following way: a highly ordered single crystalline core particle forms mostly unaffected by the polymer because the polymer is bound in the metastable intermediate precipitated earlier.[54] Once the intermediate starts dissolving, some polymer is released and adsorbs on the side faces of the growing crystals. At this point, single crystal growth is not possible anymore due to blocking of surface sites, but lamellae grow from the $\{10\bar{1}0\}$ faces of the core crystal. This suppresses the formation of hexagonal prismatic crystals at further growth. The combination of a very highly oriented and single crystalline core and the formation of the lamellar features leads to the eventually observed corn on the cob structure in the HRTEM images. The PXRD data are thus a superposition of the effect of nanocrystalline parts and large grain effects in these crystals.

Very recently, Nesper and co-workers[61] have reported the synthesis of iron oxide colloids; their data suggest that there are similarities between the growth mechanisms of the iron oxide particles and our zinc oxide particles precipitated with EO_{68}-b-SSH_{25} because both systems appear to involve varying degrees of oriented aggregation. The iron oxide particles exhibit a decrease in the coherence length along the c-axis, analogous to our data presented here. In contrast to our samples, however, they exhibit single crystalline diffraction patterns. Because the

authors did not comment in detail on the internal structure of the particles, we are not able to draw final conclusions about correlations or differences between the structure of their particles and our samples.

References and Notes

(1) Matijevic, E. *Acc. Chem. Res.* **1981**, *14*, 22.
(2) Matijevic, E. *Langmuir* **1986**, *2*, 12.
(3) Matijevic, E. *Chem. Mater.* **1993**, *5*, 412.
(4) Göltner, C. G.; Antonietti, M. *Adv. Mater.* **1997**, *9*, 431.
(5) Cölfen, H.; Antonietti, M. *Langmuir* **1998**, *14*, 582.
(6) Cölfen, H.; Limin, Q. *Chem. Eur. J.* **2000**, *7*, 106.
(7) Donners, J. J. J. M.; Heywood, B. R.; Meijer, E. W.; Nolte, R. J. M.; Roman, C.; Schenning, A. P. H. J.; Sommerdijk, N. A. J. M. *Chem. Commun.* **2000**, 1937.
(8) Marentette, J. M.; Norwig, J.; Stöckelmann, E.; Meyer, W. H.; Wegner, G. *Adv. Mater.* **1997**, *9*, 647.
(9) Qi, L. M.; Cölfen, H.; Antonietti, M. *Chem. Mater.* **2000**, *12*, 2392.
(10) Öner, M.; Norwig, J.; Meyer, W. H.; Wegner, G. *Chem. Mater.* **1998**, *10*, 460.
(11) Rieger, J.; Thieme, J.; Schmidt, C. *Langmuir* **2000**, *16*, 8300.
(12) Colfen, H. *Macromol. Rapid Commun.* **2001**, *22*, 587.
(13) Qi, L.; Cölfen, H.; Antonietti, M.; Li, M.; Hopwood, J. D.; Ashley, A. J.; Mann, S. *Chem. Eur. J.* **2001**, *7*, 3526.
(14) Bigi, A.; Boanini, E.; Cojazzi, G.; Falini, G.; Panzavolta, S. *Cryst. Growth Des.* **2001**, *1*, 239.
(15) Hartgerink, J. D.; Beniash, E.; Stupp, S. I. *Science* **2001**, *294*, 1684.
(16) Feldmann, C. *Scr. Mater.* **2001**, *44*, 2193.
(17) Feldmann, C. *Adv. Mater.* **2001**, *13*, 1301.
(18) Feldmann, C.; Metzmacher, C. *J. Mater. Chem.* **2001**, *11*, 2603.
(19) Banfield, J. F.; Welch, S. A.; Zhang, H.; Thomsen Ebert, T.; Penn, R. L. *Science* **2000**, *289*, 751.
(20) Berman, A.; Hanson, J.; Leiserowitz, L.; Koetzle, T. F.; Weiner, S.; Addadi, L. *Science* **1993**, *259*, 776.
(21) Berman, A.; Hanson, J.; Leiserowitz, L.; Koetzle, T. F.; Weiner, S.; Addadi, L. *J. Phys. Chem.* **1993**, *97*, 5162.
(22) Aizenberg, J.; Hanson, J.; Koetzle, T. F.; Weiner, S.; Addadi, L. *Chem. Eur. J.* **1995**, *1*, 414.
(23) Weiner, S.; Addadi, L. *J. Mater. Chem.* **1997**, *7*, 689.
(24) Bouropoulos, N.; Weiner, S.; Addadi, L. *Chem. Eur. J.* **2001**, *7*, 1881.
(25) Kröger, N.; Deutzmann, R.; Sumper, M. *Science* **1999**, *286*, 1129.
(26) Kröger, N.; Lehmann, G.; Rachel, R.; Sumper, M. *Eur. J. Biochem.* **1997**, *250*, 99.
(27) Heywood, B. R.; Mann, S. *Adv. Mater.* **1994**, *6*, 9.
(28) Mann, S. *J. Mater. Chem.* **1995**, *5*, 935.
(29) Mann, S.; Burkett, S. L.; Davis, S. A.; Fowler, C. E.; Mendelson, N. H.; Sims, S. D.; Walsh, D.; Whilton, N. T. *Chem. Mater.* **1997**, *9*, 2300.
(30) Falini, G.; Albeck, S.; Weiner, S.; Addadi, L. *Science* **1996**, *271*, 5245.
(31) Falini, G.; Fermani, S.; Gazzano, M.; Ripamonti, A. *Chem. Eur. J.* **1997**, *3*, 1807.
(32) Falini, G.; Gazzano, M.; Ripamonti, A. *Adv. Mater.* **1994**, *6*, 46.
(33) Falini, G.; Gazzano, M.; Ripamonti, A. *J. Cryst. Growth* **1994**, *137*, 577.
(34) Bertoni, E.; Bigi, A.; Falini, G.; Panzavolta, S.; Roveri, N. *J. Mater. Chem.* **1999**, *9*, 779.
(35) Adair, J. H.; Suvaci, E. *Curr. Opin. Colloid Interface Sci.* **2000**, *5*, 160.
(36) Fendler, J. H. *Supramol. Chem.* **1995**, *6*, 209.
(37) Fendler, J. H. *Curr. Opin. Solid State Mater. Sci.* **1997**, *2*, 365.
(38) Schwarz, K.; Epple, M. *Chem. Eur. J.* **1998**, *4*, 1898.
(39) Busch, S.; Dolhaine, H.; DuChesne, A.; Heinz, S.; Hochrein, O.; Laeri, F.; Podebrad, O.; Vietze, U.; Weiland, T.; Kniep, R. *Eur. J. Inorg. Chem.* **1999**, *10*, 1643.

(40) Hasse, B.; Ehrenberg, H.; Marxen, J. C.; Becker, W.; Epple, M. *Chem. Eur. J.* **2000**, *6*, 3679.

(41) Kawaguchi, H.; Hirai, H.; Sakai, K.; Sera, S.; Nakajima, T.; Ebisawa, Y.; Koyama, K. *Colloid Polym. Sci.* **1992**, *270*, 1176.

(42) Calvert, P.; Rieke, P. *Chem. Mater.* **1996**, *8*, 1715.

(43) Alivisatos, A. P. *Science* **2000**, *289*, 736.

(44) Penn, R. L.; Banfield, J. F. *Science* **1998**, *281*, 969.

(45) Hollemann, A. F.; Wiberg, N. *Lehrbuch der anorganischen Chemie*, 91−100 ed.; W. DeGruyter: Berlin, New York, 1985.

(46) West, A. R. *Grundlagen der Festkörperchemie*; VCH: Weinheim, 1992.

(47) Seitz, C. Ph.D. Thesis, University of Mainz, Mainz, 1999.

(48) Taubert, A.; Palms, D.; Weiss, Ö.; Piccini, M.-T.; Batchelder, D. N. *Chem. Mater.* **2002**, *14*, 2594.

(49) http://www.scioncorp.com/frames/fr_scion_products.htm.

(50) http://cimesg1.epfl.ch/CIOL/ems.html.

(51) Sagalowicz, L.; Fox, G. *J. Mater. Res.* **1999**, *14*, 1876.

(52) Warren, B. E. *X-ray Diffraction*; Dover: New York, 1990.

(53) Guinier, A. *X-ray Diffraction of Crystals, Imperfect Crystals and Amorphous Bodies*; Dover: New York, 1994.

(54) Taubert, A.; Palms, D.; Glasser, G. *Langmuir* **2002**, *18*, 4488.

(55) Rechsteiner, P.; Hulliger, J.; Flörsheimer, M. *Chem. Mater.* **2000**, *12*, 3269.

(56) Roth, S. W.; Langley, P. J.; Quintel, A.; Wübbenhorst, M.; Rechsteiner, P.; Rogin, P.; König, O.; Hulliger, J. *Adv. Mater.* **1998**, *10*, 1546.

(57) Quintel, A.; Hulliger, J. *Chem. Phys. Lett.* **1999**, *312*, 567.

(58) Quintel, A.; Hulliger, J.; Wübbenhorst, M. *J. Phys. Chem. B* **1998**, *102*, 4277.

(59) Hulliger, J.; Rogin, P.; Quintel, A.; Rechsteiner, P.; König, O.; Wübbenhorst, M. *Adv. Mater.* **1997**, *9*, 677.

(60) Williams, D. B.; Carter, C. E. *Transmission Electron Microscopy-A Textbook for Materials Science*; Plenum Press: New York, London, 1996.

(61) Niederberger, M.; Krumeich, F.; Hegetschweiler, K.; Nesper, R. *Chem. Mater.* **2002**, *14*, 78.